Advanced Intelligent Systems

ADVANCED INTELLIGENT SYSTEMS Open Access

www.advintellsyst.com

RESEARCH ARTICLE OPEN ACCESS

EMG-Driven Telemetry and Inference System for Fish: Pose Reconstruction and Flow Sensing

Rahdar Hussain Afridi[1] | Waqar Hussain Afridi[1] | Muhammad Hamza[1] | Ahsan Tanveer[1] | Mingxin Wu[1,2] | Xingwen Zheng[3,4,5] | Liang Li[6,7,8,9] | Guangming Xie[1,10]

[1]State Key Laboratory for Turbulence and Complex Systems, Intelligent Biomimetic Design Lab, School of Advanced Manufacturing and Robotics, Peking University, Beijing, China | [2]School of Mechanics and Safety Engineering, Zhengzhou University, Zhengzhou, China | [3]Institute of Cyber-Systems and Control, College of Control Science and Engineering, Zhejiang University, Hangzhou, China | [4]Institute of Fundamental and Transdisciplinary Research, Zhejiang University, Hangzhou, China | [5]State Key Laboratory of Ocean Sensing, Zhejiang University, Hangzhou, China | [6]Department of Collective Behaviour, Max Planck Institute of Animal Behavior, Konstanz, Germany | [7]Centre for the Advanced Study of Collective Behaviour, University of Konstanz, Konstanz, Germany | [8]Department of Biology, University of Konstanz, Konstanz, Germany | [9]Department of Computer and Information Science, University of Konstanz, Konstanz, Germany | [10]Institute of Ocean Research, Peking University, Beijing, China

Correspondence: Liang Li (lli@ab.mpg.de) | Guangming Xie (xiegming@pku.edu.cn)

Received: 7 September 2025 | **Revised:** 16 December 2025 | **Accepted:** 18 February 2026

Keywords: biological signal processing | electromyography (EMG) | fish locomotion | flow-regime inference | machine learning | robotic fish | telemetry

ABSTRACT

Intelligent sensing systems that integrate biological signals with machine learning open new opportunities to understand and replicate animal locomotion in natural environments. Conventional telemetry methods capture only limited variables and cannot reconstruct detailed kinematics or hydrodynamic context. An electromyography (EMG)-driven intelligent telemetry framework is introduced that decodes both body pose and environmental conditions in freely swimming fish. A custom 16-channel telemetry unit recorded intramuscular EMG synchronized with kinematics across laminar flows at multiple speeds, two Kármán vortex streets, a reverse Kármán vortex street, and free-swimming trials. A deep neural network mapped feature-augmented EMG to joint angles in a head-fixed frame, enabling midline reconstruction with sub-centimeter accuracy (∼3.8% body length) and joint angle prediction within 4° root mean squared erroFir ($R \approx 0.81$). The same pipeline classified flow regimes and discrete flow speeds with high accuracy. Channel-efficiency analysis identified mid-body axial electrodes as sufficient to capture most flow-relevant information, guiding minimizing electrode count and invasiveness. Predicted kinematics were validated through computational fluid dynamics simulations and robotic embodiment that replayed decoded swimming motions. These results establish EMG as a dual-purpose bio-signal for locomotor and environmental inference, demonstrating an AI-driven telemetry framework that links muscle activity, kinematics, and fluid interactions.

1 | Introduction

Animals achieve locomotor performance that remains difficult to reproduce in engineered systems [1, 2]. In fishes, axial musculature drives undulatory waves that generate thrust [3–6] and, in principle, conveys information about body configuration and external flow [7]. Understanding how fish muscles generate and modulate these waves is important not only for inspiring bioinspired engineering but also for advancing fundamental biology. Fish represent some of the most successful locomotor designs shaped by evolution, and their neuromuscular control strategies underpin critical ecological behaviors, such as migration, predator evasion, and energy-efficient swimming. This raises a central question: do multisite electromyograms (EMG) recorded during natural swimming contain sufficient information to infer

Rahdar Hussain Afridi and Waqar Hussain Afridi contributed equally to this work.

both whole-body kinematics and aspects of the surrounding hydrodynamic environment? Answering this question would enable telemetry that operates when vision fails (e.g., in turbid water, due to occlusion, and remote locations) and collect sufficient physiological data to provide a functional readout of the sensorimotor system during swimming, which current telemetry methods cannot achieve because they typically capture only limited physiological variables and lack inference frameworks for reconstructing movement or flow conditions.

Laboratory studies have revealed important features of fish muscle activity and swimming mechanics. EMG recordings in rainbow trout have been shown to contain critical timing, frequency, and intensity information [8], and databases linking EMG with constitutive properties have been developed for crucian carp [9]. EMG studies more broadly reveal distinct recruitment patterns: red (slow-twitch) muscles dominate steady swimming [3, 4], whereas both red and white (fast-twitch) fibers contribute to unsteady behaviors [4–6]. Posterior musculature has been shown to generate the majority of swimming power [10], and the functions of red axial muscles have been quantified across different swimming modes [11]. Studies of mackerel further highlighted the mechanical dynamics of steady swimming [12]. Other experiments demonstrated that fish can exploit vortex wakes to adopt an energetically favorable 'gait' [13–15]. These findings underscore the richness of EMG as a window into neuromuscular control, but translating laboratory insights to natural conditions remains challenging due to environmental complexity [16, 17]. Key behaviors, such as rapid C- and S-starts, which are crucial in predator–prey interactions [18, 19], also remain insufficiently explored in naturalistic contexts.

Fish kinematics are most often analyzed using video-based approaches [13, 14, 18, 20], but vision is severely limited in turbid or cluttered environments, which are typical of many natural habitats. Telemetry has therefore become indispensable in field studies [21]. Existing systems, including acoustic, radio, archival, satellite, and passive tags, can record parameters such as position, depth, acceleration, tailbeat frequency, or basic EMG [22]. However, these devices generally capture only subsets of variables at relatively low temporal resolution and cannot reconstruct full-body motion or hydrodynamic context. EMG telemetry in particular has so far been applied mainly to measure muscle activation patterns or their correlation with swimming speed [23, 24]. Its potential to decode detailed kinematics in freely swimming fish remains largely unexplored, despite the success of similar approaches in human biomechanics, where EMG has been used to predict joint angles and limb movements [25]. Fish locomotion, however, presents distinct challenges: unlike discrete-joint limb systems, fish generate continuous wave-like bending along the body [17], complicating direct pose reconstruction. Our prior work [7] demonstrated that EMG can be mapped to kinematic variables (joint angles) in laboratory flow tanks; however, no framework has yet been generalized to multiple hydrodynamic regimes or to unconstrained free-swimming conditions.

In this work, we address the challenge of extracting rich locomotor and environmental information from muscle activity by developing a unified EMG-driven telemetry framework for freely swimming fish. We purposefully customized a 16-channel archival telemetry system for EMG in koi/carp. We collected synchronized EMG and kinematics data across laminar flow, two Kármán vortex street (KVS, 5 and 7 cm cylinders), a reverse Kármán vortex street (RKVS, featuring an upstream flapping fin), and free-swimming trials. Unlike conventional approaches that provide only limited physiological data, our system combines multichannel EMG acquisition with feature-augmented deep learning to reconstruct time-resolved joint kinematics and classify hydrodynamic regimes across laminar, vortex, and free-swimming conditions. A channel-efficiency analysis further reveals that mid-body axial electrodes capture most of the flow-relevant information, offering a pathway to reduce electrode count and invasiveness for future ecological studies. To establish cross-domain validity, the decoded kinematics are not only consistent with computational fluid dynamics (CFD) simulations but can also be physically embodied in a robotic fish, demonstrating that biological muscle signals can directly generate realistic swimming motions. Together, these advances establish EMG as a dual-purpose bio-signal for movement and hydrodynamic condition inference and position our framework as an intelligent system that bridges biology, fluid mechanics, and robotics, opening new opportunities for ecological monitoring and bio-inspired design.

2 | Bio-Signal Telemetry and Modeling Framework

This section outlines a unified bio-signal framework encompassing EMG acquisition, preprocessing, feature extraction, pose construction, and learning models utilized for both kinematic regression (Section 3) and environmental classification (Section 4).

2.1 | Animals, Care, and Ethics

The Institutional Animal Care and Use Committee of Peking University approved all experimental procedures and animal care. Laboratory animal professional technical examination certificate number: TY2018466.

Koi (*C. rubrofuscus*, $N = 8$, standard length = 25.5 ± 1.67 cm, weight = 0.473 ± 0.068 kg) fish were acquired from the fish market for this work (Table 1). The fish were kept in a well-maintained tank ($2 \times 4 \times 0.3\ m^3$) with a capacity of 2400 liters of fresh water. One-third of the tank's water was replaced weekly with fresh, non-chlorinated water. The automatic feeder dispensed food for the fish three times a day. In the meantime, the fish tank's water is filtered at a rate of 6,000 liters/hour. The water temperature was controlled and kept at 20 ± 2°C. All fish were kept in the tank for 2 months after the experiment and then released into the lake with other fish.

2.2 | Fish Sedation and Body Metrics Logging

Prior to EMG electrode implantation, fish were sedated by immersion in a bath containing 160 mg L^{-1} tricaine methanesulfonate (MS-222) to minimize stress and ensure ethical handling. The solution is administered orally and exits the fish's gills, keeping the subject anesthetized throughout the electrode placement process. As the fish was anesthetized, its standard length and weight were measured.

TABLE 1 | Table of experiment for open water experiment.

	Physical parameters		Swimming conditions			
Subject	**Weight, kg**	**Length, cm**	**Circular**	**Maze**	**No obstacle**	**Flow tunnel**
1	0.505	27	✓	✓	✓	
2	0.410	24	✓	✓	✓	
3	0.475	25.5	✓	✓	✓	
4	0.36	23	✓	✓	✓	
5	0.435	24	✓	✓	✓	
6	0.505	26				✓
7	0.53	27.5				✓
8	0.565	27				✓

2.3 | EMG Telemetry Hardware and Electrode Placement

Carp exhibit carangiform locomotion, with most propulsive bending occurring over the posterior 60% of body length (BL). Accordingly, bilateral axial electrodes were implanted from 0.5 to 1.0 BL to capture muscle activity that directly drives undulation. Two reference electrodes were placed bilaterally near the gills and kept spatially separated from active sites. Channel locations are summarized in Table 2 and illustrated in Figure 1a.

Electrode fabrication and implantation: Electrodes were custom-made from 0.1 mm insulated copper wire. Approximately 10 mm of insulation was stripped from each end. For implantation, each wire was passed through a 28-gauge hypodermic needle; the distal end was bent into a small hook so that, after needle withdrawal, the wire remained anchored in the target muscle. For a single channel's differential recording, the + (positive) and – (negative) electrodes were placed above and below the lateral line. Twelve channels (Ch1–Ch12) targeted red axial musculature at six equidistant longitudinal positions per side (0.5–1.0 BL). Four additional channels (Ch13–Ch16) targeted appendicular muscles of the pectoral (left/right) and pelvic (left/right) fins. This layout captured both propulsion (axial) and steering (fins) motor systems.

Electrodes routing and stabilization: All wires were bundled, glued, and sutured to a dorsal fin ray, with minimal slack to accommodate maximum body bending. These kept wires close to the body, reduced hydrodynamic drag and motion artifacts, and improved placement stability during high-flow trials.

Archival telemetry unit and packaging: EMG was acquired with a custom 16-channel differential recorder incorporating instrumentation amplification, a 24-bit ADS1299 ADC, an ESP32-S3 microcontroller, an light-emitting diode (LED) synchronization marker, and on-board microSD storage (Figures 1b and S2). The unit measured 6.6 × 5.2 × 3.3 cm and 140 g in air; in water, it was packaged to near-neutral buoyancy using multilayer plastic sealing and a latex sleeve, with all cable exits sealed using hot-melt adhesive. For free-swimming experiments, the unit was mounted on the fish using a biocompatible cyanoacrylate (1469 SB, Vetbond). In flow-treadmill trials, the unit remained off-body, and 1 m electrodes were connected to the device. (see Movie S1)

Acquisition parameters: Signals were amplified and digitized at 1 kHz per channel (24-bit resolution) and logged as comma-separated values (CSV) files on the microSD card. The configuration supported stable, multisite intramuscular EMG recording during both flow-conditioned and free-swimming behaviors.

2.4 | Vision-Based Kinematic Data Acquisition

A Sony RX100m5 camera was used to over-the-top record the fish at 100 fps, as shown in Figure 2a,b, for its midline data. The video data undergo post-processing to ensure synchronization with the EMG signals. This process involves trimming the video footage to remove the irrelevant parts at the beginning and end of the recordings, which were identified using LED visual markers. The LED marker turns on when the EMG device starts recording and turns off when the recording stops, providing a clear reference for synchronization. Additionally, the EMG data are recorded at 1000 Hz, while the video is captured at 100 Hz. To align the two datasets, the video frame rate is upscaled to 1000 Hz to match the EMG sampling rate, ensuring precise synchronization between the two modalities.

DeepLabCut (DLC) is utilized to extract fish pose or the midline data from videos (100 fps), as shown in Figures 2a,b and 3c, and Movie M1. The DLC training dataset included 12 videos of water treadmill experiments and 14 videos of open water experiments, all featuring subjects at various swimming speeds, flow regimes, and obstacles. The videos are cropped and trimmed during preprocessing to reduce computation costs. The fish body is manually labeled with 12 evenly distributed labels along the fish midline from the eyes to the caudal fin base (caudal peduncle).

TABLE 2 | The 16 channels' (Ch) electrode placement.

L, R Electrode's BL ratios						L, R Fins Electrode's	
Ch1, Ch7	Ch2, Ch8	Ch3, Ch9	Ch4, Ch10	Ch5, Ch11	Ch6, Ch12	Ch13, Ch14	Ch15, Ch16
0.5 BL	0.6 BL	0.7 BL	0.8 BL	0.9 BL	1 BL	Pectoral Fins	Pelvic Fins

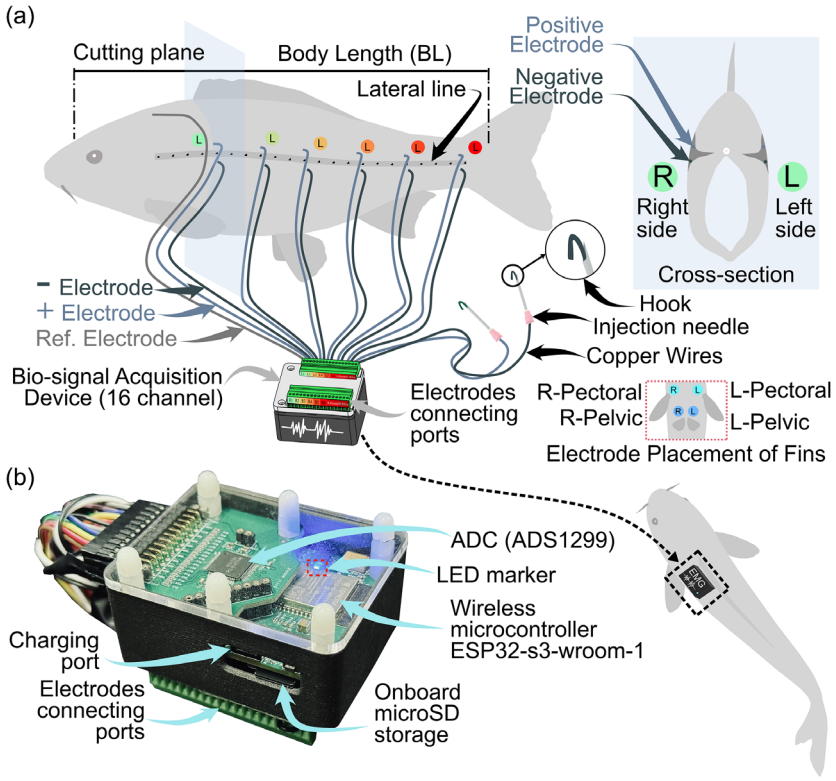

FIGURE 1 | EMG acquisition for free-swimming fish. (a) Electrode layout: fine insulated copper wire pairs implanted bilaterally to record 16 differential channels. (b) Custom 16-channel archival fish telemetry unit.

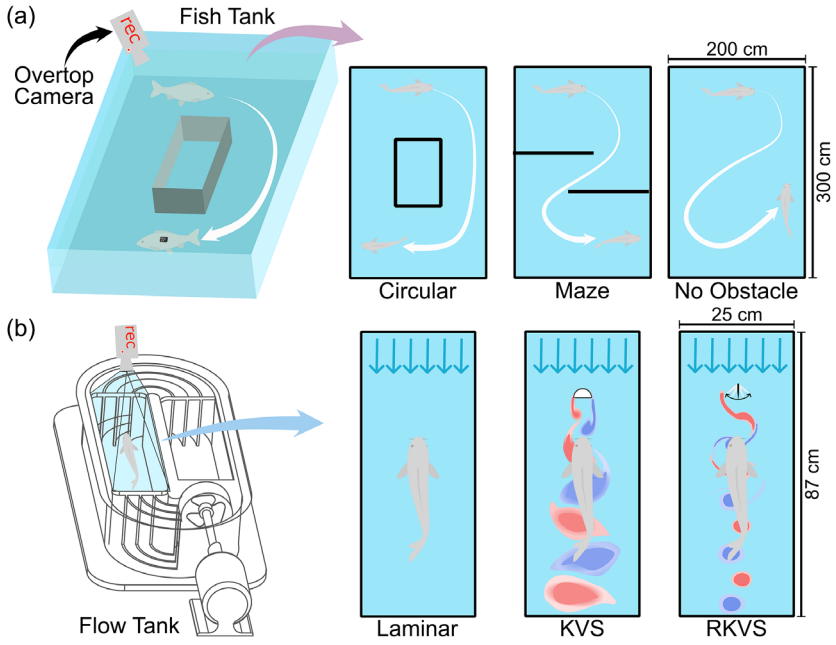

FIGURE 2 | Experimental setup for EMG and video data collection. (a) Free swimming in a tank with a circular obstacle, a maze, or no obstacle. (b) Flow-conditioned swimming in a flow tank under laminar flow, KVS, and KVS (see Appendix Figure S1).

A total of 598 frames from all videos are labeled, and the model is trained with the initial weights of the ResNet-152 backbone for 5×10^5 iterations with the default DLC settings. The fish pose data of each subject is extracted from videos using the Analyze function of DLC. The filtered DLC pose with a likelihood above 0.9 was used for the analysis, and the pose was also visually analyzed by superimposing it over the video (Movie S1). A custom-made MATLAB [26] code was developed to post-process the fish body pose data from DLC. The fish pose data from DLC are in the global space, which is transformed into the frame attached to the fish's head, as shown in Figure 3c, using Equation (1).

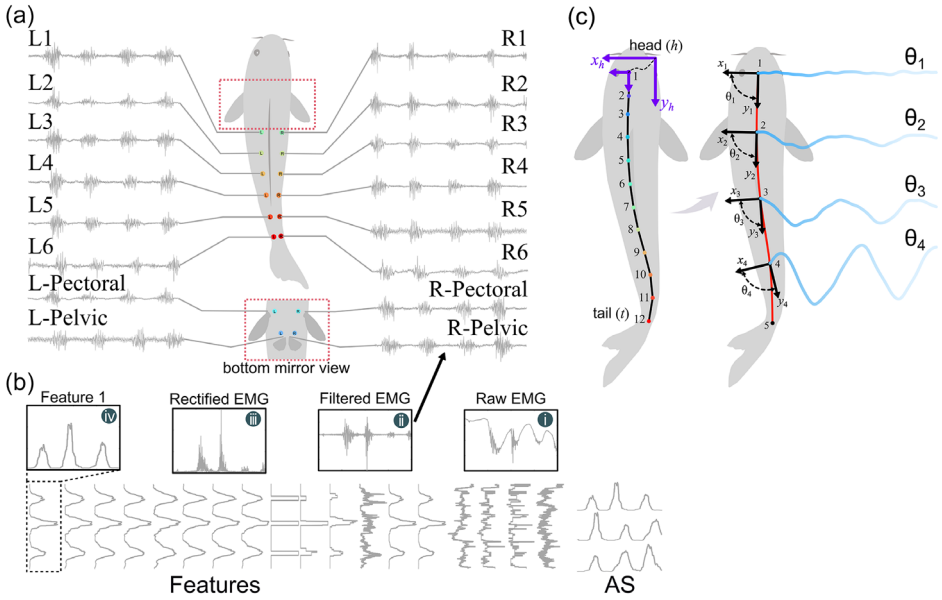

FIGURE 3 | Processing of inputs and outputs. (a) Showing filtered EMG of axial L1–L6/R1–R6 and fin (pectoral, pelvic) channels. (b) EMG preprocessing and features pipeline: band-pass filtering, rectification, and RMS with a sliding window. (c) Pose extraction and kinematic variables: DLC midline mapped to head-fixed joint angles θ_1–θ_4 via forward kinematics.

$$ {}^{i-1}H_{t,i} = \begin{bmatrix} \cos\alpha_{t,i-1} & -\sin\alpha_{t,i-1} & 0 & P_{t,x,k,i} \\ \sin\alpha_{t,i-1} & \cos\alpha_{t,i-1} & 0 & P_{t,y,k,i} \\ 0 & 0 & 1 & 0 \\ 0 & 0 & 0 & 1 \end{bmatrix} \quad (1) $$

H is the homogenous transformation matrix (HTM) used to transform the $P_{t,k}$ from global to head frame and then to local frame. Where t is the time, or the video frames $t = 0,1,2,\ldots$, up to the end frame. Where $P_{t,x,k,i} = p_{t,x,k,i-1} - d_{t,x,i}$ and $P_{t,y,k,i} = p_{t,x,k,i-1} - d_{t,y,i}$ are transformed midline points. The angle between the previous frame $i-1$ and the proceeding frame$i$ is $\alpha_{t,i-1}$, d_i is the displacement of the frame i in frame $i-1$, and p_t is the set of fish body pose vectors extracted by DLC. Frame 0 will be the global frame, and frame $i=1$ is attached to $p_{t,k=1}$, which is the head of the fish. First, all the p_k $(k = 1, 2, \ldots, 12)$ vectors are transformed to the head frame by Equation (1), which is essential because the wave is propagated from head to tail during the swimming process, and it simplifies the thought process.

The DLC pose was stable in the X-axis but stabilized in the Y-axis through Makima interpolation, generating query points, and evaluating the Makima at these query points. The pose was transformed to joint space using Equation (1), and the number of joint angles was reduced to four, allowing for the reproduction of the fish pose with equal-length segments (Figure 3c). The joint angles will be used to train a machine learning (ML) model. Later, the joint angles are transformed in the same manner to reproduce the body pose from ML model predictions.

2.5 | Experimental Protocols and Hydrodynamic Conditions

To span structured and unstructured behaviors, we collected synchronized EMG and kinematic data under two locomotor regimes: flow-conditioned swimming in a water treadmill and free-swimming in an open pool. After intramuscular implantation, fish recovered for ~30 min in water from their home tank. Datasets from all conditions were used to train and evaluate EMG-driven models across diverse hydrodynamic conditions.

2.5.1 | Free-Swimming Trials

The fish were placed in a static water pool for free-swimming trials. The experiments were designed to elicit natural behaviors by introducing three different spatial arrangements: (1) circling a square enclosed obstacle, (2) obstacle-rich environments to simulate cluttered habitats of navigating through obstacles, and (3) unrestricted open swimming (Figure 2a). This setup encouraged variable locomotor strategies and spontaneous body movements. EMG signals were collected from 16 channels, while fish kinematics were simultaneously captured from above. These trials enabled us to collect bio-signals and body posture data in the absence of external flow fields, allowing for comparison with flow-conditioned scenarios.

2.5.2 | Flow-Conditioned Trials

To simulate ecologically relevant hydrodynamic conditions, structured flow experiments were conducted in a closed-loop water treadmill (Loligo, Figure 2b, and Movie S1). The fish were exposed to five controlled water velocities, with laminar flow regimes tested at 0.146, 0.184, 0.235, and 0.274 m/s. We first measured the exact flow speed using a turbine-type flow probe (model LS300A) without fish being in the flume. These laminar flow experiments provided a baseline condition characterized by negligible turbulence. The flow was confirmed to be laminar with minimal boundary-induced distortion, as shown by 2D PIV measurements, vorticity remains below $|\omega_z| < 4^{s-1}$ throughout the field, with limited boundary effects (Movie S1). Additionally, fish were subjected to KVS generated by cylindrical obstacles of 5 and 7 cm, inducing vortex shedding that challenged the fish's motor control. Separate RKVS created by actuating a 3D-printed caudal fin at 1.5 Hz. The fin was fabricated from

Future TPU (https://www.wenext.cn/static/material/78), which complies with ISO 10993-10 and ISO 10993-5 standards for skin sensitivity and cytotoxicity, mimicking an active wake environment. The vortex shedding was visualized by dye visualization, but in the absence of this fish (Movie B1). We observed stable vortex shedding for KVS and RKVS. Each condition was repeated at the same four flow speeds to generate a diverse training dataset. The combined dataset supports both pose prediction and flow condition classification tasks using EMG inputs.

2.6 | EMG Preprocessing, Feature Extraction, and Augmentation

All EMG was post-processed offline in Python. The pipeline comprised filtering, feature extraction, stacking, and training/testing of the ML models. (Figure 3b) The data from each channel were notch-filtered at 50 Hz (mains) and band-pass filtered 20–450 Hz to suppress motion artifacts and high-frequency noise. Given the hydrodynamic forces acting on freely swimming fish, we implemented mechanical stabilization measures (bundling, gluing, and dorsal fin suturing) to minimize electrode motion relative to the musculature. Although the recordings were acute (1–2 h), we still quantitatively verified stability. (see Note S3) The signal-to-noise ratios remained high across channels (Figure S5), amplitude probability distributions were narrow and unimodal (Figure S6), EMG spectral structure was preserved across trials (Figure S7), and cross-channel correlations remained low apart from expected anatomical adjacency (Figure S8). Such consistency across independent metrics indicates that electrode migration, drift, or intermittent contact did not materially affect the recordings, ensuring that EMG decoding performance reflects neural–muscular activity rather than artifact. Filtering examples are shown in Figure 3bi–ii.

Furthermore, for each channel j, we computed 18 features (Figure 3b). The time-domain features included variance, root mean sqaure (RMS), integrated EMG, mean absolute value, log detector, waveform length, average amplitude change, absolute standard deviation, zero crossings, Willison amplitude, and Myopulse percentage rate [27]. Frequency-domain features: frequency ratio, mean power, total power, mean frequency, median frequency, and peak frequency. A time–frequency descriptor was also included (short-time time–frequency estimate) [7].

$$F_j = \begin{bmatrix} f_{1,1,j} & f_{2,1,j} & \cdots & f_{18,1,j} \\ f_{1,2,j} & f_{2,2,j} & \cdots & f_{18,2,j} \\ f_{1,3,j} & f_{2,3,j} & \cdots & f_{18,3,j} \\ \vdots & \vdots & \ddots & \vdots \\ f_{1,n,j} & f_{2,n,j} & \cdots & f_{18,n,j} \end{bmatrix} \tag{2}$$

F_j given in Equation (2) are features extracted from channel the j^{th}. Where $j = 1, 2, 3, \ldots, 16$ is the number of channels, and $n = 1, 2, \ldots$, the length of the signal. F_j is populated by features (f) extracted with a feature sliding window FSW = 300 samples (0.30 s at 1 kHz) with 1-sample stride. The population of F_j is an iterative process and repeated for all 18 features, resulting in F_j with shape $(n \times 18)$ shown in Figure 4a.

$$S_j = \begin{bmatrix} s_{1,j} & s_{2,j} & \cdots & s_{\text{ASW},j} \\ s_{2,j} & s_{3,j} & \cdots & s_{1+ASW,j} \\ s_{3,j} & s_{4,j} & \cdots & s_{2+\text{ASW},j} \\ \vdots & \vdots & \ddots & \vdots \\ s_{n,j} & s_{n+1,j} & \cdots & s_{n+\text{ASW},j} \end{bmatrix} \tag{3}$$

To enrich the representation of muscle activation beyond traditional handcrafted features matrix F_j, we augmented the feature

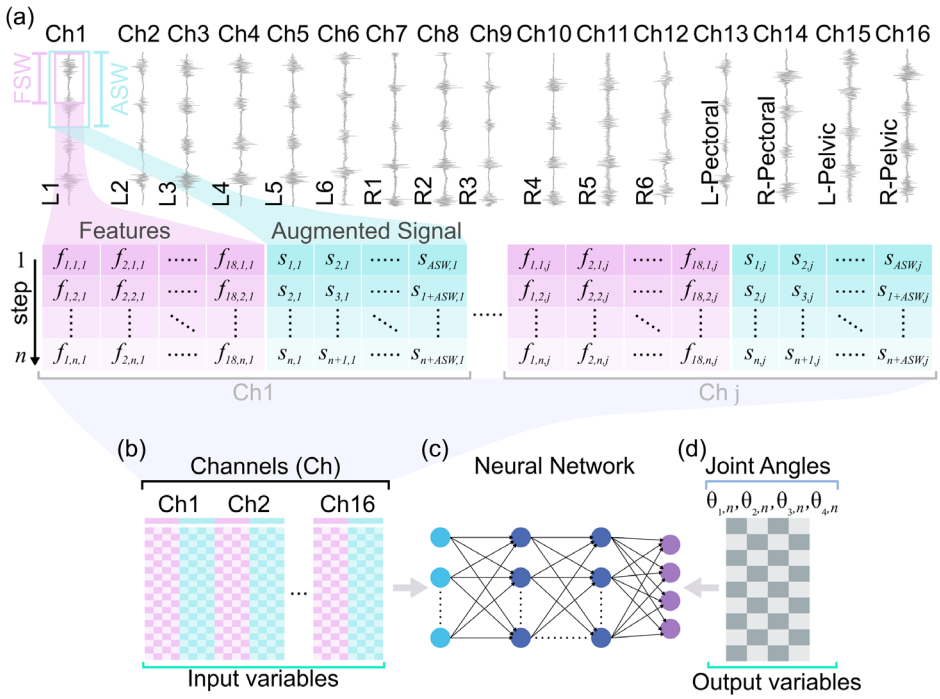

FIGURE 4 | Overview of input–output generation for neural network. (a) Feature extraction and augmentation. (b) Augmented matrices are stacked to create the input variables. (c) A DNN maps the multichannel input to (d) the joint angles θ_1–θ_4.

matrix for each channel by concatenating an RMS overlapping subsequences matrix (S_j). The S_j matrix is constructed by creating overlapping subsequences of channel j RMS feature with an augmentation sliding window ASW of size (400 samples or milliseconds, step size of 1). This augmentation process resulted in a matrix, referred to as the RMS overlapping subsequences matrix (S_j), given by Equation (3). Unlike traditional augmentation methods, this augmentation preserved the original signal length by applying the sliding window without smoothing or averaging. Each EMG channel was thus represented by a matrix of shape $n \times ASW$, where n is the length of the EMG signal, and ASW is the window size. The final augmented input matrix for each channel was then formed by horizontally concatenating the 18 extracted features and the RMS overlapping subsequences matrix.

Unlike conventional data augmentation approaches (which focus on increasing dataset size through synthetic signal generation, such as additive noise, magnitude warping, or wavelet perturbation [28]), our method performs input-level augmentation by enriching the representational content of each time step. This strategy captures both statistical abstractions and temporally localized morphology in a single matrix, allowing for a richer learning signal without altering class balance or label structure. Prior studies have shown that combining envelope-level EMG information with handcrafted features improves performance in both classification and kinematic estimation tasks [27]. Moreover, using the moving-mean signal instead of raw segments improves robustness by suppressing high-frequency noise while preserving the morphological trends essential for muscle activation decoding.

$$A_j = [F_j|S_j] = \begin{bmatrix} f_{1,1,j} & f_{2,1,j} & \cdots & f_{18,1,j} & s_{1,j} & s_{2,j} & \cdots & s_{ASW,j} \\ f_{1,2,j} & f_{2,2,j} & \cdots & f_{18,2,j} & s_{2,j} & s_{3,j} & \cdots & s_{1+\mathrm{ASW},j} \\ f_{1,3,j} & f_{2,3,j} & \cdots & f_{18,3,j} & s_{3,j} & s_{4,j} & \cdots & s_{2+\mathrm{ASW},j} \\ \vdots & \vdots & \ddots & \vdots & \vdots & \vdots & \ddots & \vdots \\ f_{1,n,j} & f_{2,n,j} & \cdots & f_{18,n,j} & s_{n,j} & s_{n+1,j} & \cdots & s_{n+\mathrm{ASW},j} \end{bmatrix} \quad (4)$$

For each channel j, the F_j and S_j are stacked($[F_j|S_j]$) into an augmented matrix of features and is given by Equation (4), with the shape of (n, (18+ ASW)) is also shown in Figure 4a.

$$V_{input} = [F_1|S_1|F_2|S_2|\ldots|F_{12}|S_{12}] \quad (5)$$

Similarly, V_{input} is the input variables matrix, which is formed by stacking all EMG channels F_j and S_j, giving it shape (n, (12(18+ASW))), as shown in Figure 4b and given by Equation (5).

The pose data from DLC are transformed to a fish's local space (head-attached frame) and to the joint space to reduce the number of parameters. The whole midline of the fish is divided into four angles with equal-length segments, and each angle is computed in the local frame. The angles are stacked together as given in Equation (6):

$$V_{output} = \begin{bmatrix} \theta_{1,1} & \theta_{2,1} & \theta_{3,1} & \theta_{4,1} \\ \theta_{1,2} & \theta_{2,2} & \theta_{3,2} & \theta_{4,2} \\ \theta_{1,3} & \theta_{2,3} & \theta_{3,3} & \theta_{4,3} \\ \vdots & \vdots & \vdots & \vdots \\ \theta_{1,n} & \theta_{2,n} & \theta_{3,n} & \theta_{4,n} \end{bmatrix} \quad (6)$$

The stacked angles matrix V_{output} each row is considered a step of the input variables ($n \times 4$), as shown in Figure 4d as output variables (V_{output}) and given by Equation (6).

2.7 | Learning Models and Training

To map EMG activity to fish body kinematics, we implemented a deep feedforward neural network trained on a rich input matrix derived from multisite intramuscular EMG recordings. Each EMG channel was processed to extract 18 handcrafted time, frequency, and time–frequency domain features, which were concatenated with a 400-sample smoothed waveform segment to form an augmented EMG matrix of shape ($n \times 418$) per channel—with 12 axial muscle channels resulted in a final input matrix of shape ($n \times 5016$), capturing both low-frequency muscle activation patterns and high-resolution statistical descriptors across the entire body. The output target was a set of four joint angles (θ_1–θ_4), computed from the fish midline in a head-attached coordinate system, representing body pose with shape ($n \times 4$).

The neural network consisted of eight fully connected layers with progressively decreasing width: [4096, 4096, 2048, 2048, 512, 512, 128, 4], each followed by a *tanh* activation except for the final linear output layer. This tapered architecture was first designed to capture high-dimensional muscle synergies and then to distill them into a compact representation of the resulting body motion. The model was trained using a custom loss function called the prediction fit index (PFI), which penalizes normalized prediction error relative to the natural variability of the ground truth. Additionally, biologically relevant bounded-error metrics (namely, the proportions of predictions within 10%, 20%, and 30% of the true joint angles) were used to assess model accuracy across diverse swimming behaviors.

3 | Evaluation of the Bio-Signal-Driven Framework's Kinematics Prediction

We implemented a simple two-step analysis strategy to assess the correlation between EMG signals and fish kinematics. First, we extracted body pose data from DLC, enabling the calculation of relevant joint angles. Subsequently, we employed the ML model to predict the fish's joint angles using the processed EMG. Then, we computed the body pose and all the parameters relevant to the predicted body pose. We are correlating the predicted and measured kinematics along with the concerned parameters. Thus, by employing this strategy, we compare and correlate predicted and measured kinematics, ultimately revealing the underlying relationship between fish EMG activity and kinematics. Model training and validation relied on laboratory datasets (water treadmill and large-tank free-swimming), since ground-truth kinematics are not feasible to obtain in the field. The onboard form factor, channels layout, and EMG feature/augmentation pipeline

remain directly deployable in field conditions, with only the ground-truthing step requiring laboratory constraints.

3.1 | Joint Angles

We evaluated the effectiveness of a deep neural network (DNN) in predicting fish body joint angles and whole-body pose using 12-channel intramuscular EMG signals recorded under diverse hydrodynamic conditions. The model was trained on a comprehensive dataset encompassing laminar flow, vortex shedding, and free-swimming scenarios, thereby capturing the full spectrum of neuromuscular responses and kinematic variability observed in naturalistic fish locomotion. A comprehensive features augmented matrix of multiple EMG channels forms an input matrix, which is then provided to a DNN. The DNN is trained to accurately predict four primary joint angles (θ_1–θ_4) characterizing the fish's midline posture. These angles sufficiently describe the body undulations observed in carangiform swimming, enabling reconstruction of the fish's swimming motion with high accuracy. Quantitative evaluation of the model's predictions (Figure 5) demonstrated robust mapping from EMG to kinematics across all tested conditions. The mean RMSE for joint angle prediction was 4 ± 1.4°, which is 8.6% of maximum lateral bending angles, with a corresponding mean Pearson correlation coefficient (R) of 0.813 ± 0.11 and a coefficient of determination (R^2) of 0.65 ± 0.183 (Figure 5c–e).

3.2 | Body Pose Reconstruction

It is of significance that we reproduce the fish body pose because it will help us visually study the fish and decode more data/parameters regarding the test subject. A custom-made MATLAB [26] code is employed to compute the fish kinematics and the following parameters, except for the CFD results. Consequently, the predicted angles are transformed through forward kinematics employing Equation (1) to produce the fish body pose in the frame attached to the head (Figure 5). The fish swimming for one tail-beat cycle of 0.612 s is shown in Figure 6d. The fish's body bends laterally in a wave form, and the tip of the deflected curve is the tail, thus producing thrust to move forward, as illustrated in Figure 6d. The body pose or midline points are interpolated with makima, as shown in Figure 6d, to produce a smooth midline, and later this smooth midline will help in the convergence of the CFD simulation. Notably, the reconstructed midline pose achieved an RMSE of 0.98 ± 0.34 cm, which is 3.84% of the mean stand length of the fish (Figure 5f), indicating a high-fidelity recovery of the overall body posture. Predictive performance was strongest in laminar flow at intermediate swimming speeds. However, it remained consistently high even under turbulent and free-swimming conditions, underscoring the generalizability and robustness of the EMG-driven model.

Direct EMG-to-kinematics decoding has been extensively studied in humans but is rarely investigated in nonhuman animals. Recent reviews of continuous (regression) EMG decoding in humans report typical joint-angle RMSE on the order of 3°–10° with correlation (R^2) values ~0.6–0.95, depending on joint, task, and algorithm [25]. Against that backdrop, our angle RMSE of 4 ± 1.4° (8.6% of max bend), Pearson's $R = 0.813 \pm 0.11$, and $R^2 = 0.65 \pm 0.183$ are squarely in the performance

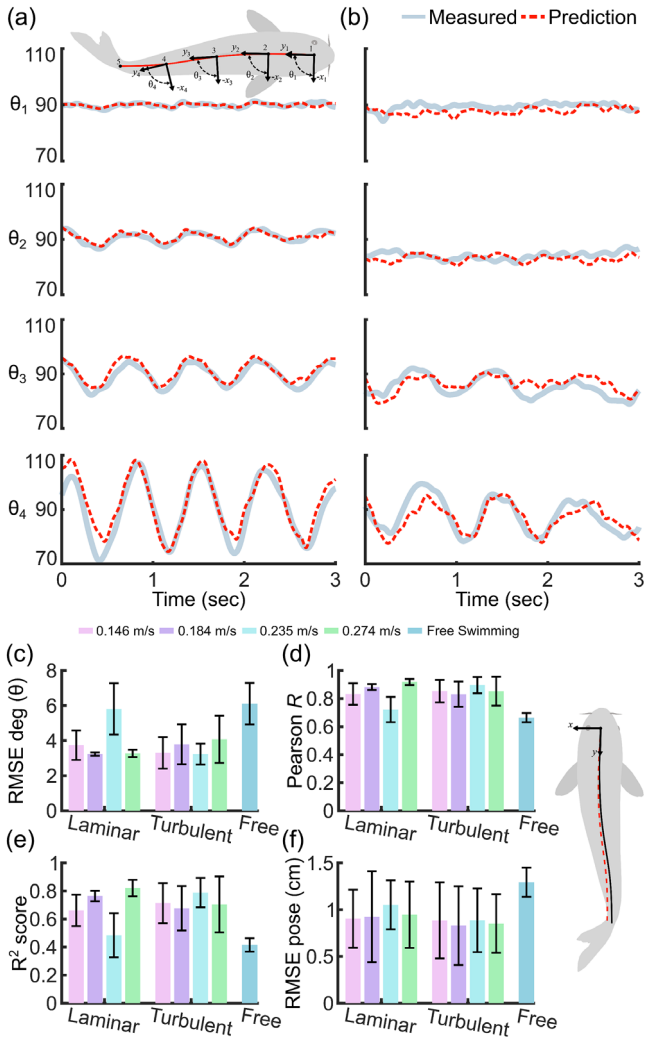

FIGURE 5 | EMG-based neural network prediction of fish kinematics. Measured (blue) and predicted (red dashed) joint angles (θ_1–θ_4) in (a) laminar flow and (b) free swimming. Performance metrics for angle prediction across conditions: (c) RMSE, (d) Pearson correlation coefficient (R), and (e) coefficient of determination (R^2). (f) RMSE of reconstructed whole-body pose (midline) in centimeters.

envelope of state-of-the-art human studies, despite the added complexity of a continuously flexible, aquatic body and variable external flow. Importantly, most prior animal telemetry studies link EMG to speed, tail-beat frequency, or qualitative activity rather than reconstructing joint angles and the entire midline. A robustness analysis of reconstruction errors further demonstrated that performance was stable across individuals and hydrodynamic conditions. Joint-angle RMSE values showed a narrow distribution, with 95% of predictions below 7.07°, while pose errors remained below 1.46 cm for 95% of all frames (Note S2; Table S1). The corresponding histograms and cumulative distribution functions (Figure S4) illustrate the absence of extreme errors or catastrophic failures, confirming the reliable generalization of the EMG-to-kinematics decoder. Our previous laminar-only study demonstrated EMG-based pose reconstruction in a flow tank [7]; the present work extends EMG-driven pose reconstruction to multiple flow regimes and to free swimming in a large tank, utilizing 12 intramuscular differential channels to continuously decode four joints. To our knowledge, cross-species

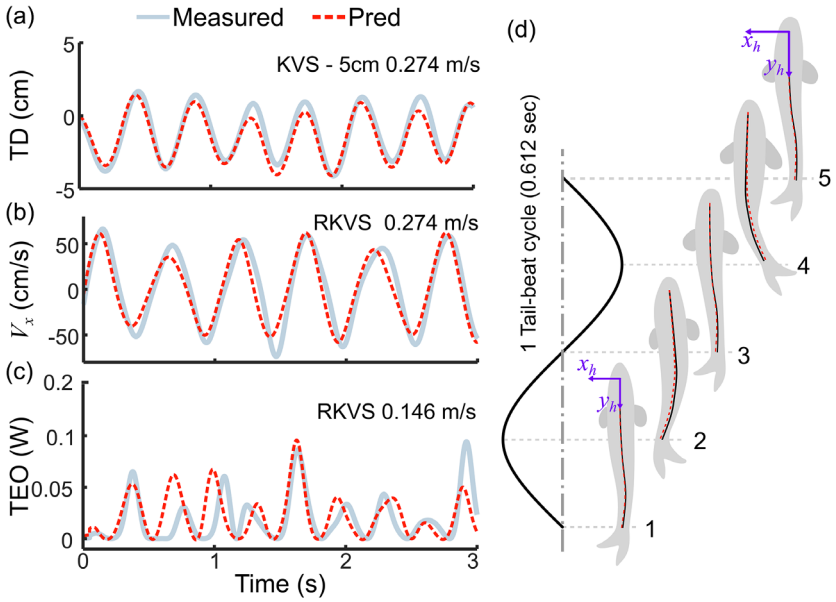

FIGURE 6 | Applications of EMG-based body pose reconstruction: (a) tail displacement (TD) in KVS (5 cm cylinder) at 0.274 m/s, (b) lateral tail velocity (V_y) in RKVS at 0.274 m/s, and (c) total energy output (TEO) estimated by Lighthill's model in RKVS at 0.146 m/s. Measured data (blue) and predictions (red dashed) are shown.

demonstrations that recover full body pose from EMG during unconstrained swimming are scarce; outside of fish, non-human EMG studies more often estimate torques or single-joint angles in constrained terrestrial tasks.

To facilitate like-for-like benchmarking, we summarize the salient axes for comparison:

- Sensing and Channels: 12-channel intramuscular differential EMG (this work) vs. 2–16 surface/intramuscular channels (typical human studies).
- Output Quantity: Four joint angles → full midline pose (this work) vs. single-joint angles or joint moments (common in human literature).
- Environment: Laminar, vortex-shedding, and free-swimming regimes (this work) vs. largely steady, gravity-dominated terrestrial tasks.
- Performance: 4° angle RMSE; pose RMSE 0.98 cm (3.84% SL); Pearson's $R \approx 0.81$; $R^2 \approx 0.65$ across regimes.
- Generalization: Trained and tested across multiple hydrodynamic conditions; midline robustness demonstrated in both flow-tank and large-tank settings.

Collectively, these results indicate that multichannel EMG, combined with a DNN, can recover time-resolved, whole-body kinematics in a nonmammalian aquatic model with errors comparable to those in leading human limb studies, while operating under substantially more variable external dynamics. This closes a gap between electrophysiological telemetry and quantitative body pose in freely swimming fish, establishing a practical baseline for future real-time telemetry, control, and energetics.

Nonhuman studies that combine EMG and kinematics largely report correlative relationships (e.g., hummingbird pectoralis EMG vs. wingbeat kinematics; trout pectoral fin EMG vs. fin trajectories) rather than decoding pose from EMG [29, 30]. By contrast, kinematic prediction in animals has been demonstrated from neural signals recorded in the spinal cord or cortex (cat hindlimb; macaque arm), not from EMG [31]. EMG-driven musculoskeletal models exist for dogs and cats, but these utilize EMG to estimate forces or moments in physics-based simulations rather than directly reconstructing joint angles [32]. To our knowledge, our study is the first to recover multisegment joint angles and full midline pose from EMG alone in a freely swimming vertebrate, and to do so across multiple flow regimes, extending beyond prior single-regime animal demonstrations.

3.3 | Derived Metrics From Pose: Tail Displacement, Lateral Velocity, and Total Energy Output

Once the body pose was reconstructed from EMG-predicted joint angles, we extended the analysis to higher-order kinematic and energetic quantities to demonstrate the broader utility of the framework. A custom MATLAB [26] code was developed to compute the tail lateral displacement (TD), the tail-tip velocity (V_x), and the total energy output (TEO). Figure 6 presents three representative applications. Carp and koi fish are carangiform swimmers during steady or straight-line swimming, undulating approximately 60% of their bodies. Carangiform swimmers produce thrust as the propulsive wave is propagated along the fish's body and transfers the moment by the tail displacement to the surrounding water, resulting in a reaction force that pushes the swimmer. We can compute the displacement at several points along the fish's midline; however, the displacement at the tail is important because the tail generates the majority of thrust [33]. Additionally, we can extract classical swimming kinematic parameters, such as tailbeat amplitude and frequency, from the TD. In Figure 6a, the TD is extracted from the body pose of a fish swimming in the KVS flow regime with a 5 cm cylinder at 0.274 m/s.

Fish tail-beat velocity is an important parameter that should be calculated because it is used to study various aspects of fish (such as

fish tail thrust or propulsive force generation, the relationship between tail-beat velocity and swimming speed, to assess the health and well-being of fish in aquaculture settings, and the impact of environmental stressors on fish populations). Moreover, lateral tail-tip velocity (V_x) was obtained by temporal differentiation, as shown in Figure 6b for RKVS at 0.274 m/s. This variable captures the oscillatory dynamics that drive thrust production and is typically inaccessible with conventional telemetry tags.

Fish use propulsive force to move forward, backward, turn, and maneuver around obstacles. The generation of propulsive force depends on the morphology of the species. Carp fish can produce propulsive force through their pectoral fins, body, and tail. However, the majority of the propulsive force is produced by the tail, so for the sake of simplification, we will compute the tail propulsive force. The propulsive force in this study is calculated using the large-amplitude elongated-body theory, as implemented in the book "Fish Swimming" [34] with minor adjustments for our specific case. The instantaneous velocity vector is decomposed into two components; V_t the component tangential, while V_p perpendicular to the tail surface.

$$V_t = V_x \sin\ \vartheta + V_y \cos\ \vartheta$$

$$V_p = V_x \cos\ \vartheta - V_y \sin\ \vartheta$$

where is $\vartheta = \theta^{\circ}_{tail} - 90°$. θ°_{tail} is the output variable ML model. V_x is the tail lateral velocity while V_y forward swimming speed of fish. The fish's swimming speed is known from the water treadmill flow speed at which the experiment was conducted. There is a mass of water around the tail, which is pushed by the tail in the direction of the vector V_p acting as an added or virtual mass, which is incorporated as M with an assumption that the tail movement will have an impact on the water flow in a circular area around it.

$$M = \rho_w\, a_{tail}$$

where ρ_w is the density of water and $a_{tail} = l^2 \frac{\pi}{4}$ is the area around the tail incorporating the virtual or added mass. The propulsive force of the tail is given by:

$$F = MV_tV_y \sin\ \vartheta + \frac{1}{2} MV_p^2 \cos\ \vartheta$$

The instantaneous TEO of the fish is the product of the fish's instantaneous forward-moving velocity V_y and propulsive force (F) is given by:

$$E = V_y \times F$$

Figure 6c shows the instantaneous TEO generated by the tail for 3 sec. The resulting TEO traces showed close agreement with experimental measurements, underscoring the potential of this bio-signal–driven approach to connect neuromuscular activity with kinematics and energetics of swimming.

3.4 | Computational Fluid Dynamics (CFD) Analysis

The CFD analysis is conducted in COMSOL 6.1 [35] on a real fish 2D profile extracted by a 3D scanner (Shining 3D EaScan-Q130) from the test subject at IBDL. The fish body is divided into 10 joints, and the joints are undulated with ML prediction. We simulated the Reynolds-averaged Navier–Stokes equations (assuming constant fluid properties) in an incompressible fluid environment using COMSOL's transient time analysis to understand the unsteady flow around a real fish profile. The k-ε turbulence model is used for the CFD simulations. The fluid selected is water, with a constant density $\rho = 998.2\ \mathrm{kg/m^3}$ and a constant kinematic viscosity $\nu = 1.0034 \times 10^{-6}\ \mathrm{m^2/s}$. The medium is considered steady still while the fish is moving forward with an average velocity of 0.467 m/s in the Y-axis direction. The far-field walls have been kept at a distance of approximately 22.5 times the fish's length to minimize wall effects. The boundary condition at the far-field walls is no-slip. The total number of mesh elements is approximately 3.2×10^4. The Reynolds number is 0.34 million. Moreover, the dynamic mesh feature is activated using the diffusion method, and the smoothing and remeshing options are employed to capture the fish's locomotion.

Furthermore, we can study the real fish's hydrodynamics using the predicted kinematics by simulating it in CFD, as shown in Figure 7 and Movie S1. The ML predictions were used to simulate the real fish in CFD for 15 s. As shown in Figure 7a, the vorticity of the vortices is high near the caudal fin and lower as they move away from the caudal fin. Additionally, Figure 7b shows three different pressure regions on each side of the fish body from the head to the end of the caudal fin when the fish is undulating. The pressure regions are arranged in a high-low-high or low-high-low pattern, resulting in a vortex street. Moreover, the velocity of the fluid, as shown in Figure 7c, is high in the vortices newly generated near the end of the caudal fin. The vortices lose momentum as they move away, resulting in a decrease in vorticity and velocity.

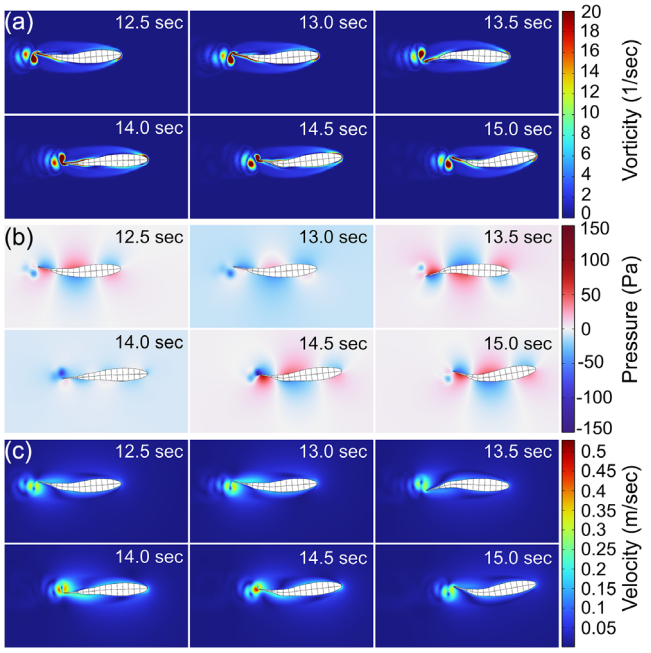

FIGURE 7 | Validation of EMG-based body angle predictions through CFD simulations and robotic replication. (a) Vorticity field generated by simulating fish body undulations predicted by the DNN model trained on EMG signals. (b) Corresponding pressure field showing distribution along the predicted body pose. (c) Velocity field illustrating hydrodynamic flow induced by the predicted kinematics.

Moreover, Figure 7c shows velocity plots at different time steps, and it can be seen that vortices generate high-momentum flows. The velocity of the fluid, as shown in Figure 7c, is high in the vortices newly generated near the end of the caudal fin. The vortices lose momentum as they move away, resulting in a decrease in vorticity and velocity. These results, obtained through CFD simulations, demonstrate the potential to correlate fish muscle EMG activity (reflecting the wave motion of the fish body) with hydrodynamic phenomena in fish swimming.

3.5 | Open-Loop EMG-Driven Robotic Fish Actuation

To extend the applicability of the bio-signal–driven framework beyond computational validation, we implemented an open-loop robotic actuation pipeline. Multichannel EMG data recorded from the axial muscles of freely swimming fish were processed through the trained neural network to predict joint angles (θ_1–θ_4). These predicted kinematics were then converted into pulse-width modulation (PWM) signals using a calibrated mapping and stored on a Raspberry Pi Zero W. An onboard Python-based controller sequentially replayed the PWM commands to drive three servo motors (S1–S3) embedded in a soft-bodied robotic fish with a morphology similar to its biological counterpart.

Figure 8a illustrates this process: EMG signals were preprocessed, fed into the neural network, and converted into PWM commands for the robotic fish. Time-lapse frames (Figure 8b) show the robotic platform reproducing undulatory swimming patterns consistent with the decoded biological kinematics (Movie S1, for 15 s). Although the current implementation is open-loop (replaying precomputed motor commands without sensory feedback), it provides embodied evidence that the EMG-to-motion framework directly generates actionable motor signals. While this study does not aim to replicate specific biological phenomena, the same approach could be applied similarly to prior robotic studies investigating fish behavior and fluid–structure interactions [15]. Unlike CFD, which evaluates consistency at the fluid-dynamics level, robotic embodiment demonstrates that EMG-derived kinematics can be physically realized as locomotor motion. This confirms that the telemetry-to-kinematics pipeline yields signals suitable for both computational analysis and physical reproduction, offering a complementary tool for comparative biology and bio-inspired robotics.

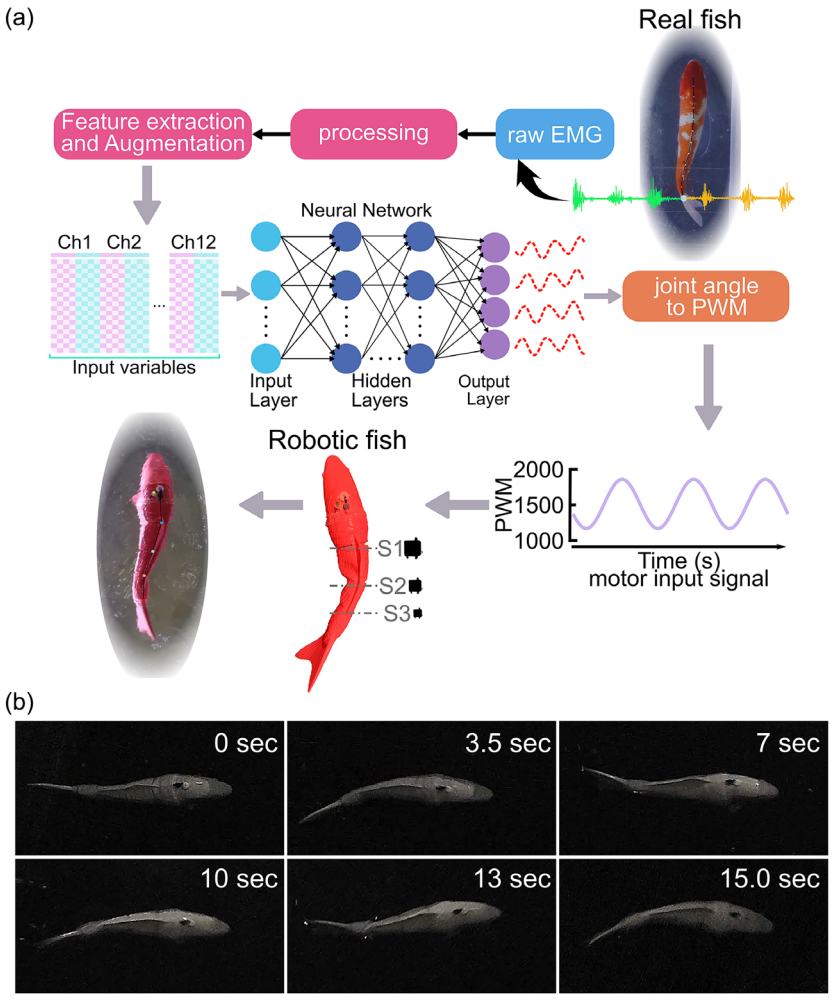

FIGURE 8 | Open-loop EMG-driven robotic actuation. (a) Pipeline: EMG features are processed by a neural network to predict joint angles, which are then mapped to PWM signals for servo-motor control in a robotic fish. (b) Representative time-lapse frames showing the robotic fish reproducing undulatory swimming motions from decoded EMG data.

4 | Hydrodynamic Condition Inference with the EMG-Driven Framework

In this section, we test whether EMG signals encode flow-specific neuromuscular responses by reusing the same bio-signal pipeline developed for kinematic decoding (Section 2 and Section 3) to classify hydrodynamic conditions and flow speeds. Multichannel EMG collected from distinct anatomical regions is preprocessed and featurized identically to Section 2; the network architecture is unchanged except that the regression head that outputs joint angles is replaced with a softmax classification head (Figure 9a). To place the deep network's performance in context, we also evaluated three classical machine-learning models trained on the same EMG feature set: Support Vector Machines, Random Forests, and k-Nearest Neighbors. Their implementation details and full quantitative comparison with the DNN are provided in Note S1, with classification accuracies and confusion matrices summarized in Figure S3. These complementary analyses confirm that while classical models extract meaningful flow-related structure from EMG, the DNN provides substantially higher accuracy and robustness across hydrodynamic regimes. Using these inputs, the model predicts environmental class labels for flow regime (Laminar, KVS-5, KVS-7 cm, RKVS) and discrete flow speeds (FS1–FS4). This yields a unified telemetry pipeline that infers both what the fish is doing (joint kinematics) and where it is swimming (hydrodynamic context) from the same EMG data. In this work, "hydrodynamic condition inference" refers to the classification of externally imposed flow regimes and speeds from EMG patterns that covary with the hydrodynamic environment; it does not imply active sensory perception by the musculature.

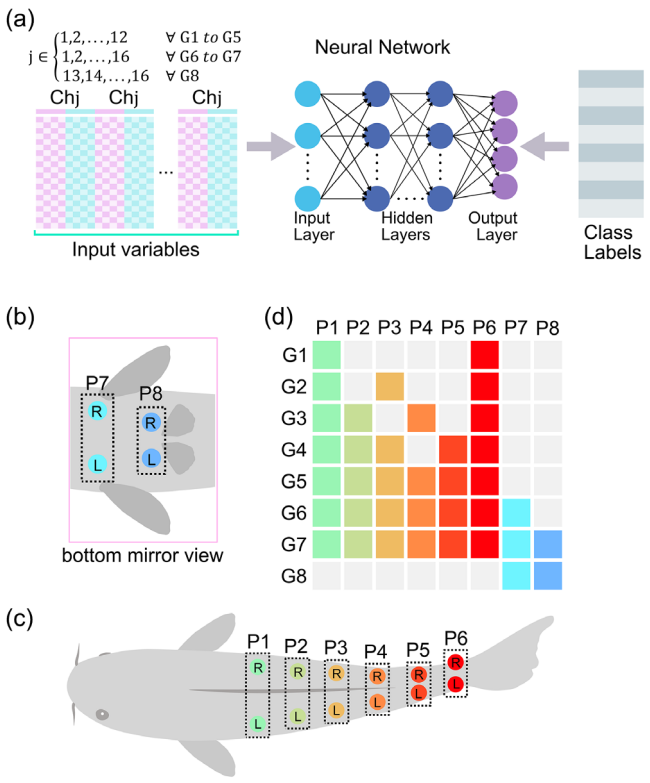

FIGURE 9 | EMG-based classification setup. (a) The feature matrix from selected channels is input to a fully connected DNN for flow/speed classification. (b) Bottom-view placements for pectoral (P7) and pelvic (P8) fin channels. (c) Axial channels placements at six longitudinal positions (P1–P6). (d) Definition of eight channel groups (G1–G8) used for ablation across anatomical regions.

4.1 | From Kinematics to Flow Condition Discrimination: Reusing the EMG-Driven Framework for Flow Classification

We assessed how neuromuscular activity encodes environmental conditions by classifying flow speed and hydrodynamic regime from multichannel EMG. To assess the contribution of different muscle regions to predicting flow conditions, we organized the channels into pairs (P1–P8) spanning both appendicular and axial musculature (Figure 9b,c). Specifically, the pair P7 corresponded to the pectoral fin muscles and P8 to the pelvic fin muscles (Figure 9b), while P1–P6 represented six longitudinal positions along the axial musculature (Figure 9c). The pairs were grouped as (G1–G8), and each group provides a subset of channels for ablation-style comparisons (Figure 9d). The features extracted from these regions were fed into a fully connected DNN consisting of an input layer, several hidden layers, and an output layer for classifying environmental conditions (Figure 9a).

The output labels comprised four discrete (i) flow speeds (FS1–FS4) or (ii) hydrodynamic regimes (Laminar, KVS-5, KVS-7 cm, RKVS) for Channel-Efficient Classification and fourteen output labels of flow speed × regime for Generalized Classifier. Grouping channels by anatomy (axial vs. fins) allows us to quantify where environmental signatures are most prominent, while keeping the modeling constant. This design cleanly tests whether axial propulsion muscles or appendicular steering muscles better encode flow and speed and provides a principled basis for channel-efficient telemetry. The same network architecture and training protocol were used across G1–G8 so that any performance differences reflect information content of the anatomical region, not model capacity. Classification accuracy and confusion matrices are summarized in Figures 10 and 11.

4.2 | Channel-Efficient Classification: Accuracy and Channel Selection

We reuse the same bio-signal pipeline from Section 2 and train the classifier on feature matrices computed from selected EMG channels. Eight anatomical groupings (G1–G8; Figure 9b–d) enable ablation across axial and fin muscle regions. With the full pairs group (particularly G7), confusion matrices show strong diagonal dominance for both flow speed (FS1–FS4) and hydrodynamic regime (Laminar, KVS-5, KVS-7 cm, RKVS), reflecting robust separability of conditions (Figure 10c,d). That these results are obtained using a consistent DNN architecture underscores that the accuracy differences indeed reflect the underlying information of each anatomical region, rather than model tuning.

Ablation results reveal a consistent pattern: mid-to-posterior axial groups (G3–G5) achieve approximately 80% accuracy for both speed and regime classification, while fin-only (G8) performs worst (Figure 10a,b). This suggests that the axial propulsion musculature carries richer information about the surrounding flow environment than the appendicular steering muscles. Such a finding aligns with classical biomechanical understanding: axial musculature functions as the primary

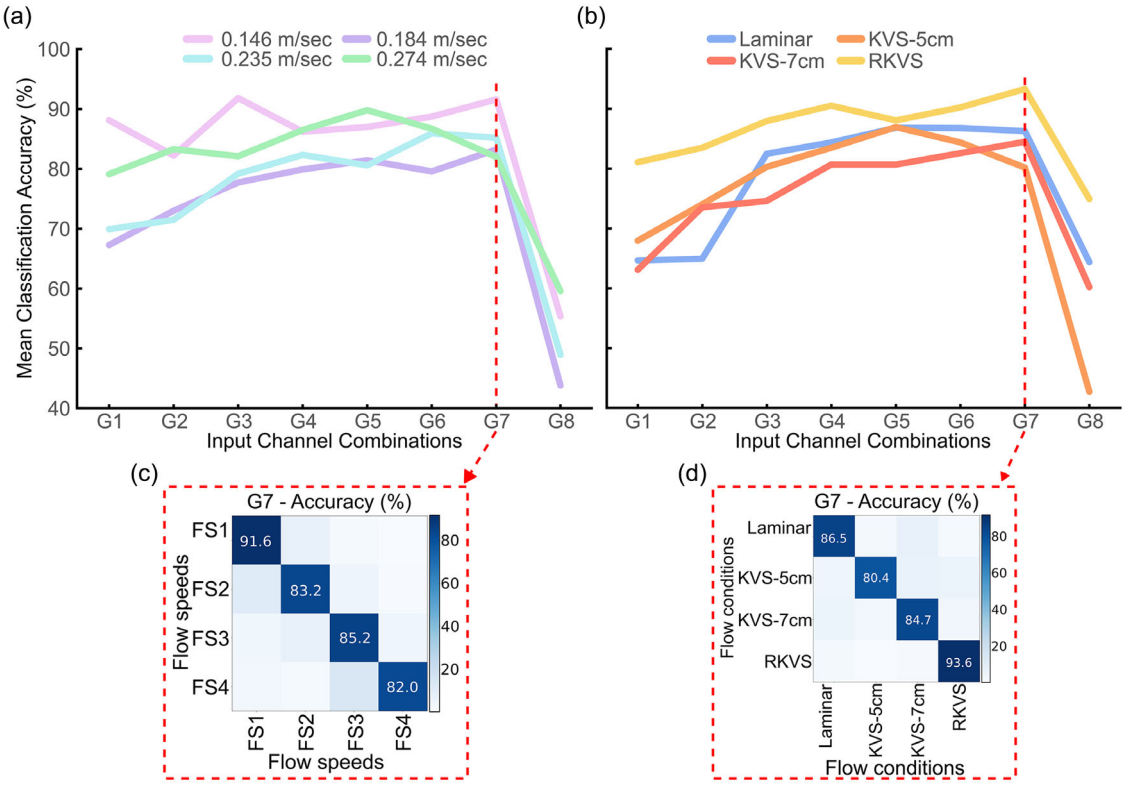

FIGURE 10 | EMG-based classification performance. Mean accuracy by channels grouping (G1–G8) for (a) flow-speed classes FS1–FS4 (0.146, 0.184, 0.235, and 0.274 m/s) and (b) hydrodynamic regimes. The confusion matrix for using channel group G7 for the (c) flow-speed and (d) hydrodynamic-regime.

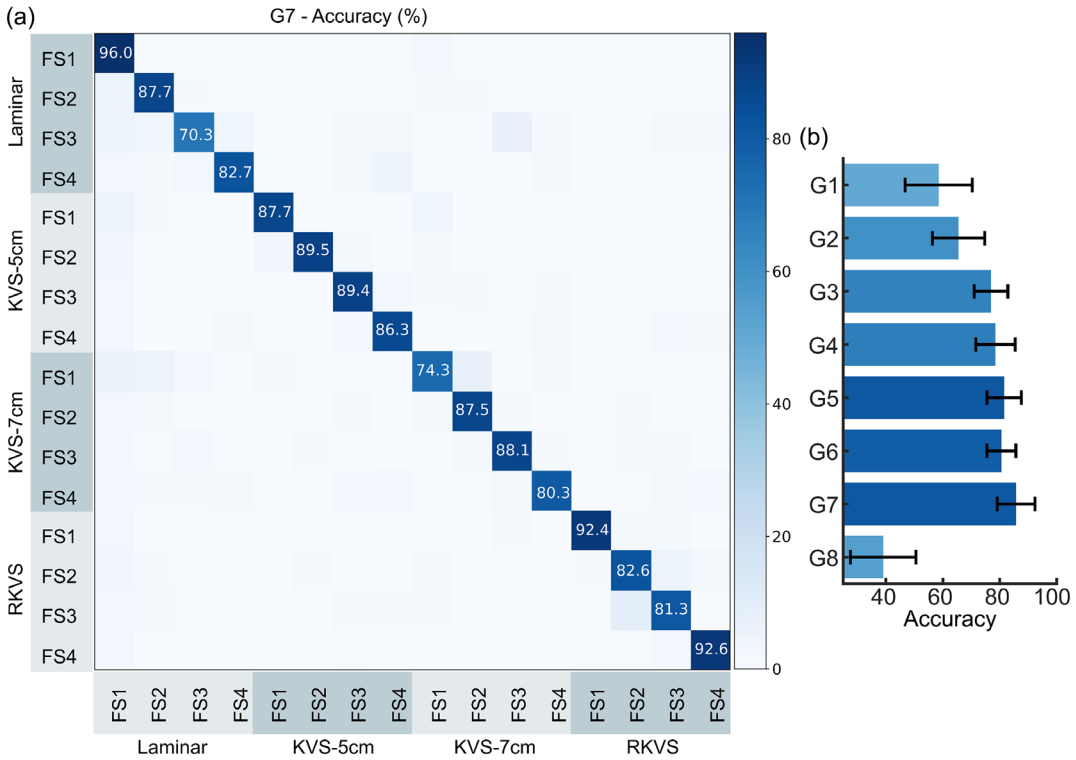

FIGURE 11 | Generalized EMG classification of environment and speed. (a) Confusion matrix for full-channel configuration (G7). (b) Mean ± SD accuracy across channels groups G1–G8.

locomotive engine in fishes, particularly in generating thrust [3, 4, 4–6] and responding adaptively to flow, whereas fin muscles play more modulatory or stabilizing roles [29, 36]. Indeed, axial muscles serve as the "plesiomorphic locomotor engine" in vertebrates, and retain a central role in locomotion across taxa [37]. Moreover, in computational studies of undulatory swimming, the posterior axial muscles bear the brunt of torque and power generation, consistent with their central role in producing responsive forces in flowing environments [38]. Accuracy is typically highest for laminar and turbulent conditions, with G3–G5 providing the most consistent predictions. This reinforces the notion that these axial regions not only register muscular output but also do so differentially across flow regimes, effectively encoding environmental signatures in neuromotor patterns [7].

Overall, this task-driven configuration highlights a practical, channel-efficient approach: mid-body axial sensors capture the majority of perceptual signatures related to environmental flow, while fin channels contribute minimally to classification accuracy. By integrating evidence from vertebrate biomechanics and computational models of fish locomotion, our findings establish a robust interpretative framework: axial muscles, especially those along the mid-to-posterior body, not only drive motion but also encode subtle environmental cues, making them ideal loci for flow monitoring systems and biologically inspired telemetry.

Task-focused channel selection. Based on the ablations in Figure 10a,b:

- Speed only: a single mid-body axial group (e.g., G4) is sufficient; two to three adjacent groups (G3–G5) approach full-channel accuracy. Fin channels are unnecessary.
- Regime only (Laminar, KVS-5, KVS-7 cm, RKVS): start with G3–G5; add a posterior axial set (e.g., G6) when distinguishing KVS-5 vs KVS-7 cm is critical.
- Fin-only (G8) provides the lowest accuracy and is not recommended for generalized decoding.

These recommendations provide a practical recipe for channel-efficient telemetry: axial sensors at mid-body locations are the most informative for both speed and regime, and fin channels contribute little to classification accuracy.

4.3 | Generalized Classifier for All Regimes and Speeds (Full-Channel G7)

We trained a single generalized classifier to simultaneously decode both flow regime and flow speed. Using the full-channel configuration (G7), the confusion matrix (Figure 11a) shows strong diagonal dominance with only occasional off-diagonal entries, primarily between adjacent speeds and between KVS-5 and KVS-7 cm. This indicates that neuromuscular responses contain robust, class-specific signatures that generalize across the combined task.

Ablations across channel groups confirm the channel–accuracy trade-off (Figure 11b). Mean accuracies for G1–G8 were 58.58%, 65.53%, 76.92%, 78.49%, 81.53%, 80.57%, 85.73%, and 39.09%, respectively; G7 (all channels) achieved the highest accuracy. Thus:

- Combined speed + regime (single model): use an axial array spanning P1–P6 or the G3–G5 core for a compact, low-power configuration with a small accuracy trade-off; G7 maximizes accuracy when channel count is not a constraint.
- Tight hardware/surgical budget: deploy G4 first; expand to G3–G5 if needed.

This provides a practical recipe for channel-efficient telemetry: select G7 for comprehensive flow-state classification, or G3–G5 when minimizing implants, power, or bandwidth.

While the proposed EMG-driven framework demonstrates the feasibility of decoding multi-joint kinematics and environmental conditions in freely swimming fish, several limitations should be acknowledged. First, ground-truth kinematic labels relied on laboratory flow-tank and camera-based measurements, which are not available in natural field deployments, thereby constraining validation to quasi-controlled environments. Second, the telemetry device was externally mounted on the fish. Although the unit was carefully packaged and wrapped in a latex sleeve to achieve near-neutral buoyancy and reduce hydrodynamic resistance, some additional drag may still have been introduced, potentially subtly influencing swimming kinematics. Third, the present modeling relied on offline training and open-loop robotic replication; real-time closed-loop telemetry and control remain future challenges. Finally, the study was conducted on individuals within a single species, and generalization across species remains to be tested. Addressing these limitations will be critical for translating this framework into robust ecological and bio-inspired robotics applications.

5 | Conclusion and Future Work

This study demonstrated that intramuscular EMG can recover time-resolved body pose and classify hydrodynamic context in freely swimming fish. Using a 16-channel telemetry unit and a neural decoding pipeline, four joint angles were predicted with a mean RMSE $\approx 4°$ ($R \approx 0.81$; $R^2 \approx 0.65$), and midline pose was reconstructed with $\approx$0.98 cm RMSE ($\sim$3.8% BL) across a range of swimming conditions. The same signals classified flow regimes and discrete flow speeds with high accuracy. These results establish a direct link between neuromuscular activity, kinematics, and environmental interactions, providing a quantitative framework for studying locomotion in naturalistic conditions.

A key contribution for biologists and marine researchers is the channel-efficiency analysis, which showed that axial channels encode most of the flow-relevant information. This finding offers practical guidance for reducing electrode count, minimizing invasiveness, and facilitating long-term ecological monitoring. More broadly, the proposed framework demonstrates how bio-signal–driven telemetry can unify biological sensing, kinematic modeling, and hydrodynamic validation, with applications in both ecological research and bio-inspired robotics. Future work will focus on reducing the size of the telemetry unit to minimize drag and on extending the framework to real-time closed-loop decoding and cross-species validation.

Author Contributions

Rahdar Hussain Afridi: conceptualization, investigation, methodology, formal analysis, writing – original draft, and writing – review and editing. **Waqar Hussain Afridi**: conceptualization, investigation, methodology,

formal analysis, writing – original draft, and writing – review and editing. **Muhammad Hamza**: methodology, formal analysis, and writing – review and editing. **Ahsan Tanveer**: conceptualization, investigation, methodology, formal analysis, writing – original draft, and writing – review and editing. **Mingxin Wu**: formal analysis and writing – review. **Liang Li**: conceptualization, methodology, formal analysis, supervision, and writing – review and editing. **Guangming Xie**: conceptualization, methodology, formal analysis, funding acquisition, resources, project administration, supervision, and writing – review and editing. All authors contributed to and agreed with the content of the final version of the manuscript.

Acknowledgments

This work was supported in part by the National Natural Science Foundation of China under Grant U22A2062, Grant U23B2037, Grant 12272008, Grant W2442039, and Grant 61973007 and in part by the Beijing Natural Science Foundation under Grant 3242003. Xingwen Zheng gratefully acknowledges the funding from the Natural Science Foundation of Zhejiang Province (Grant No. LZ25F030002).

Open Access funding enabled and organized by Projekt DEAL.

Funding

This work was supported in part by the National Natural Science Foundation of China under Grant U22A2062, Grant U23B2037, Grant 12272008, Grant W2442039, and Grant 61973007 and in part by the Beijing Natural Science Foundation under Grant 3242003. Furthermore, L.L. acknowledges funding support from the Max Planck Society, the Deutsche Forschungsgemeinschaft (DFG, German Research Foundation) under Germany's Excellence Strategy-EXC 2117–422037984, DFG project number 462886202, the Sino-German Centre in Beijing for generous funding of the Sino-German mobility grant M-0541, and Messmer Foundation Research Award.

Conflicts of Interest

The authors declare no conflicts of interest.

Data Availability Statement

The data that support the findings of this study are available from the corresponding author upon reasonable request.

References

1. A. J. Ijspeert, "Biorobotics: Using Robots to Emulate and Investigate Agile Locomotion," *Science (1979)* 346 (2014): 196.

2. S. A. Burden, T. Libby, K. Jayaram, S. Sponberg, and J. M. Donelan, "Why Animals Can Outrun Robots," *Science Robotics* 9 (2024): eadi9754.

3. L. C. Rome, P. T. Loughna, and G. Goldspink, "Muscle Fiber Activity in Carp as a Function of Swimming Speed and Muscle Temperature," *American Journal of Physiology-Regulatory, Integrative and Comparative Physiology* 247, no. 2 (1984): R272-R279.

4. T. P. Johnson, D. A. Syme, B. C. Jayne, G. V. Lauder, and A. F. Bennett, "Modeling Red Muscle Power Output during Steady and Unsteady Swimming in Largemouth Bass," *American Journal of Physiology-Regulatory, Integrative and Comparative Physiology* 267 (1994): R481-R488, https://doi.org/10.1152/ajpregu.1994.267.2.R481.

5. L. C. Rome and A. A. Sosnicki, "Myofilament Overlap in Swimming Carp. II. Sarcomere Length Changes During Swimming," *American Journal of Physiology. Cell Physiology* 260 (1991): C289–C296.

6. S. M. Kashin, A. G. Feldman, and G. N. Orlovsky, "Different Modes of Swimming of the Carp, *Cyprinus carpio* L.," *Journal of Fish Biology* 14 (1979): 403.

7. R. H. Afridi, W. H. Afridi, M. Hamza, et al., "Beyond Propulsion: Muscle Proprioception Enables Hydrodynamic Sensing in Fish Body," *Proceedings of the Royal Society B* 292 (2025): 20250474, https://doi.org/10.1098/rspb.2025.0474.

8. J. M. Wakeling, M. Kaya, G. K. Temple, I. A. Johnston, and W. Herzog, "Determining Patterns of Motor Recruitment during Locomotion," *Journal of Experimental Biology* 205 (2002): 359.

9. Z. Meng, Y. Xiezhen, and T. Binggang, "An Experimental Investigation into Electromyography, Constitutive Relationship and Morphology of Crucian Carp for Biomechanical "Digital Fish," *Science China Physics, Mechanics and Astronomy* 54.5 (2011): 966.

10. L. C. Rome, D. Swank, and D. Corda, "How Fish Power Swimming," *Science (197)* 261 (1993): 340.

11. J. L. Van Leeuwen, M. J. M. Lankheet, H. A. Akster, and J. W. M. Osse, "Function of Red Axial Muscles of Carp (Cyprinus carpio): Recruitment and Normalized Power Output During Swimming in Different Modes," *Journal of Zoology* 220 (1990): 123.

12. R. E. Snadwick, J. F. Sieffensen, S. L. Katz, and T. Knower, "Muscle Dynamics in Fish During Steady Swimming," *American Zoologist* 38, no. 4 (1998): 755–770, https://doi.org/10.1093/icb/38.4.755.

13. O. Akanyeti and J. C. Liao, "A Kinematic Model of kármán gaiting in Rainbow Trout," *Journal of Experimental Biology* 216 (2013): 4666.

14. J. C. Liao, D. N. Beal, G. V. Lauder, and M. S. Triantafyllou, "The Kármán Gait: Novel Body Kinematics of Rainbow Trout Swimming in a Vortex Street," *Journal of Experimental Biology* 206 (2003): 1059.

15. L. Li, M. Nagy, J. M. Graving, J. Bak-Coleman, G. Xie, and I. D. Couzin, "Vortex Phase Matching as a Strategy for Schooling in Robots and in Fish," *Nature Communications* 11 (2020): 1.

16. S. Reebs, *Fish Behavior in the Aquarium and in the Wild* (Cornell University Press, 2019).

17. A. Farrell, *Encyclopedia of Fish Physiology: From Genome to Environment* (Academic press, 2011).

18. D. Weihs, "The Mechanism of Rapid Starting of Slender Fish," *Biorheology* 10 (1973): 343.

19. Spierts, L. Y. Igor, Swimming and muscle structure in fish. Wageningen University and Research (1999).

20. L. Li, L.-M. Chao, S. Wang, O. Deussen, and I. D. Couzin, "RoboTwin: A Platform to Study Hydrodynamic Interactions in Schooling Fish," *IEEE Robotics & Automation Magazine* 31, no. 1 (2024): 10–17, https://dpo.org/10.1109/MRA.2023.3348303.

21. E. B. Thorstad, A. H. Rikardsen, A. Alp, and F. Økland, "The Use of Electronic Tags in Fish Research–An Overview of Fish Telemetry Methods," *Turkish Journal of Fisheries and Aquatic Sciences* 13 (2013): 881.

22. S. J. Cooke, E. B. Thorstad, and S. G. Hinch, "Activity and Energetics of Free-swimming Fish: Insights from Electromyogram Telemetry," *Fish and Fisheries* 5 (2004): 21.

23. Y. Makiguchi, Y. Konno, K. Konishi, et al., "EMG Telemetry Studies on Upstream Migration of Chum Salmon in the Toyohira River, Hokkaido, Japan," *Fish Physiology and Biochemistry* 37 (2011): 273.

24. P. R. Almeida, I. Póvoa, and B. R. Quintella, "Laboratory protocol to calibrate sea lamprey (Petromyzon marinus L.) EMG signal output with swimming," in *Developments in Fish Telemetry: Proceedings of the Sixth Conference on Fish Telemetry Held in Europe* (Springer), (2007): 209–220.

25. S. P. Sitole and F. C. Sup, "Continuous Prediction of Human Joint Mechanics Using EMG Signals: A Review of Model-Based and Model-Free Approaches," *IEEE Transactions on Medical Robotics and Bionics* 5 (2023): 528.

26. The MathWorks Inc, *MATLAB Version: 9.12.0.1884302 (R2022a)* (MathWorks Inc, 2022).

27. A. Phinyomark, P. Phukpattaranont, and C. Limsakul, "Feature Reduction and Selection for EMG Signal Classification," *Expert Systems with Applications* 39 (2012): 7420.

28. P. Tsinganos, B. Cornelis, J. Cornelis, B. Jansen, and A. Skodras, "Data Augmentation of Surface Electromyography for Hand Gesture Recognition," *Sensors* 20 (2020): 4892,

29. B. J. Gibbs, O. Akanyeti, and J. C. Liao, "Kinematics and Muscle Activity of Pectoral fins in Rainbow Trout (Oncorhynchus mykiss) Station Holding in Turbulent Flow," *Journal of Experimental Biology* 227 (2024): jeb246275.

30. D. L. Altshuler, K. C. Welch, B. H. Cho, et al., "Neuromuscular Control of Wingbeat Kinematics in Anna's Hummingbirds (*Calypte Anna*)," *Journal of Experimental Biology* 213 (2010): 2507.

31. Y. Fathi and A. Erfanian, "Decoding Bilateral Hindlimb Kinematics From Cat Spinal Signals Using Three-Dimensional Convolutional Neural Network," *Frontiers in Neuroscience* 16 (2022): 801818.

32. M. Galli, M. Tarabini, A. P. Moorhead, et al., "Development of a Canine Rigid Body Musculoskeletal Computer Model to Evaluate Gait," *Frontiers in Bioengineering and Biotechnology* 8 (2020): 150.

33. W. H. Afridi, A. Tanveer, R. H. Afridi, et al., "Bio-to-Robot Transfer of Fish Sensorimotor Dynamics via Interpretable Model," *Advanced Intelligent Systems* 000 (2025): e202501117, https://doi.org/10.1002/aisy.202501117.

34. J. J. Videler, *Fish Swimming* (Springer Science & Business Media, 1993), Vol. 10.

35. C. AB and others, COMSOL Multiphysics v. 6.1, Stockholm, Sweden (2023). www.comsol.com.

36. J. C. Liao and O. Akanyeti, "Fish Swimming in a Kármán Vortex Street: Kinematics, Sensory Biology and Energetics," *Marine Technology Society Journal* 51 (2017): 48.

37. N. Schilling, "Evolution of the Axial System in Craniates: Morphology and Function of the Perivertebral Musculature," *Frontiers in Zoology* 8, no. 1 (2011): 4.

38. G. Leclercq, P. Lefèvre, and G. Blohm, "3D kinematics Using Dual Quaternions: Theory and Applications in Neuroscience," *Frontiers in Behavioral Neuroscience* 7 (2013): 7.

Supporting Information

Additional supporting information can be found online in the Supporting Information section. **Supporting Figure S1**: Experimental setup for controlled flow trials. (a) Custom setup. (b) Side and (c) top views of the commercial swim tunnel (Loligo Systems, L = 87 cm, W = 25 cm) featuring a closed-loop propeller-driven flow and collimators for uniform laminar conditions. Additional details: https://www.loligosystems.com. **Supporting Figure S2**: Component of archival telemetry unit (FreeBCI-BT-16, Nanjing Chengpu Electronic Technology Co., Ltd.). **Supporting Figure S3**: Comparison of flow-condition classification across models. Confusion matrices for (a) Random Forest, (b) SVM, and (c) KNN classifiers evaluated on EMG features across laminar, KVS-5 cm, KVS-7 cm, and RKVS conditions. (d) Overall classification accuracy for DNN, SVM, Random Forest, and KNN models. **Supporting Figure S4**: Distribution of reconstruction errors across all fish, speeds, and flow regimes. (a) Histogram of joint-angle RMSE values. (b) Cumulative distribution function (CDF) of joint-angle RMSE, showing the proportion of predictions below each error threshold. (c) Histogram of midline pose RMSE values. (d) CDF of pose RMSE. RMSE values were computed relative to synchronized ground-truth kinematics. Histograms illustrate the frequency of error magnitudes, while CDFs provide a probability-based characterization of robustness. Together, these plots show that both angle and pose errors remain tightly bounded and free of extreme outliers. **Supporting Figure S5**: Per-channel Signal-to-Noise Ratio (SNR). Mean SNR (black line) and standard deviation (gray region) across all EMG channels. **Supporting Figure S6**: Amplitude probability density functions for all EMG channels. Probability density estimates of raw EMG amplitudes for each channel. The narrow, unimodal distributions reflect stable recording conditions, with no amplitude collapse or multimodal structure indicative of intermittent loss of electrode contact. **Supporting Figure S7**: Power spectral density (PSD) of EMG signals across channels. PSD curves illustrating the broadband spectral profile characteristic of intramuscular EMG. The preserved spectral shape across channels and absence of abnormal low-frequency elevation demonstrate that hydrodynamic loading and body bending did not introduce motion artifacts associated with electrode migration. **Supporting Figure S8**: Cross-channel correlation (crosstalk) matrix. Correlation matrix quantifying pairwise relationships among EMG channels. Low off-diagonal values and localized anatomical clustering reflect the expected spatial organization of muscle activity. The stable correlation structure indicates that electrode spacing and orientation remained consistent throughout recording. **Supporting Table S1**: Summary of joint-angle and pose reconstruction error statistics across 51 swimming trials. RMSE values were computed for each trial and aggregated across all fish and flow conditions. Mean, median, 95th percentile, and maximum errors quantify overall accuracy and the robustness of extreme errors for both joint-angle predictions and midline pose reconstruction.

Biographies

Rahdar Hussain Afridi received his Ph.D. in general mechanics and foundation of mechanics from Peking University, Beijing, China, and his M.Eng in mechanical engineering from Xi'an Jiaotong University, Xi'an, China. He earned his B.Sc. in mechanical engineering from CECOS University, Peshawar, Pakistan. He is currently an algorithm engineer at FAW South (Shenzhen) Technology Development Co., Ltd., where he works on humanoid robot manipulation, with a focus on training robots to interact with and manipulate objects. His research interests include robotics, biomechanics, bio-signal processing, machine learning, system identification, soft robotics, and bio-inspired underwater robotic systems.

Waqar Hussain Afridi is a Ph.D. student in general and fundamental mechanics with the school of advanced manufacturing and robotics, Peking University, Beijing, China. He received the M.Eng in mechanical engineering from Xi'an Jiaotong University, Xi'an, China, in 2021, and the B.Sc. degree in mechanical engineering from CECOS University, Peshawar, Pakistan, in 2018. His research interests include robotics, biomechanics, bio-signal processing, machine learning, system identification, soft robotics, and bio-inspired underwater robotic systems.

Muhammad Hamza is a Ph.D. student in general and fundamental mechanics with the school of advanced manufacturing and robotics, Peking University, Beijing, China. He received the M.Eng in mechanics from Xi'an Jiaotong University, Xi'an, China, in 2021, and B.Sc. degree in aerospace engineering from Institute of Space Technology, Islamabad, Pakistan, in 2018. His research interests include fluid dynamics, underwater energy harvesting, soft robotics, and bio-inspired underwater robots.

Ahsan Tanveer is a Ph.D. student in mechanics at Peking University working in the Intelligent Biomimetic Design Lab. He previously served as a lecturer at Air University and holds an M.S. in mechanical engineering from Ghulam Ishaq Khan Institute of Engineering Sciences and Technology. His research interests include soft robotics, bio-inspired underwater robots, robotic manipulation, and machine learning for control systems.

Mingxin Wu is a Research Associate Professor with the school of mechanics and safety engineering, Zhengzhou University, Zhengzhou, China. He received his master's degree in mechanical engineering from Wuhan University, Wuhan, China, in 2020, and his Ph.D. in general mechanics and foundation of

mechanics from Peking University, Beijing, China, in 2024. His research interests include bio-inspired robots, mechanism design, and soft robots.

Xingwen Zheng is a tenure-track professor (under the Hundred Talents Program) at Zhejiang University. His research interests include underwater robots, bio-inspired robots, and biomimetic sensory systems. He has published papers (including 5 cover articles) in journals such as Nature Communications, IEEE Transactions on Robotics, Advanced Functional Materials, Advanced Science, IEEE/ASME Transactions on Mechatronics, and Soft Robotics, as well as conferences such as IROS, ICRA, MEMS, Transducers, etc. He has published two academic books. He was the recipient of >20 awards. He serves as an associate editor for the IEEE Transactions on Robotics.

Liang Li is a Group Leader (PI) at the Max Planck Institute of Animal Behavior and the University of Konstanz. He received a bachelor's degree in automation from Chongqing University in 2011 and a Ph.D. in general mechanics and foundation of mechanics from Peking University in 2017. From February 2017 to June 2024, he was a postdoctoral research fellow and project leader in the department of collective behaviour, Max Planck Institute of Animal Behavior, Konstanz, Germany. His research interests include bio-inspired robots, swarm robots, collective behaviour in hybrid animal-robot systems, and bio-fluid dynamics in fish schools.

Guangming Xie received his bachelor's degrees in applied mathematics and electronic and computer technology, his master's degree in control theory and control engineering, and his Ph.D. in control theory and control engineering from Tsinghua University, Beijing, China, in 1996, 1998, and 2001, respectively. He is currently a Professor of dynamics and control with the School of Advanced Manufacturing and Robotics, Peking University, Beijing. His research interests include smart swarm theory, biomimetic robots, and deep learning.